Coronal Elemental Abundances in Solar Emerging Flux Regions

Deborah Baker, David H Brooks, Lidia Van Driel-Gesztelyi, Alexander G. James, Pascal Démoulin, David Long, Harry P Warren, David R Williams

CrossMark

Coronal Elemental Abundances in Solar Emerging Flux Regions

Deborah Baker[1] , David H. Brooks[2] , Lidia van Driel-Gesztelyi[1,3,4] , Alexander W. James[1,3] , Pascal Démoulin[3] ,
David M. Long[1] , Harry P. Warren[5] , and David R. Williams[6]

[1] University College London, Mullard Space Science Laboratory, Holmbury St. Mary, Dorking, Surrey, RH5 6NT, UK; deborah.baker@ucl.ac.uk
[2] College of Science, George Mason University, 4400 University Drive, Fairfax, VA 22030, USA
[3] Observatoire de Paris, LESIA, UMR 8109 (CNRS), F-92195 Meudon, France
[4] Konkoly Observatory of the Hungarian Academy of Sciences, Budapest, Hungary
[5] Space Science Division, Naval Research Laboratory, Washington, DC 20375, USA
[6] European Space Agency/ESAC, E-28692 Villanueva de la Cañada, Madrid, Spain

Abstract

The chemical composition of solar and stellar atmospheres differs from the composition of their photospheres. Abundances of elements with low first ionization potential (FIP) are enhanced in the corona relative to high-FIP elements with respect to the photosphere. This is known as the FIP effect and it is important for understanding the flow of mass and energy through solar and stellar atmospheres. We used spectroscopic observations from the Extreme-ultraviolet Imaging Spectrometer on board the *Hinode* observatory to investigate the spatial distribution and temporal evolution of coronal plasma composition within solar emerging flux regions inside a coronal hole. Plasma evolved to values exceeding those of the quiet-Sun corona during the emergence/early-decay phase at a similar rate for two orders of magnitude in magnetic flux, a rate comparable to that observed in large active regions (ARs) containing an order of magnitude more flux. During the late-decay phase, the rate of change was significantly faster than what is observed in large, decaying ARs. Our results suggest that the rate of increase during the emergence/early-decay phase is linked to the fractionation mechanism that leads to the FIP effect, whereas the rate of decrease during the later decay phase depends on the rate of reconnection with the surrounding magnetic field and its plasma composition.

Key words: Sun: abundances – Sun: corona – Sun: evolution – Sun: magnetic fields

Supporting material: animations

1. Introduction

Element abundance patterns have long been used as tracers of physical processes throughout astrophysics. The benchmark reference for all cosmic applications is the solar chemical composition. The observed variation in coronal solar and stellar abundances depends on the first ionization potential (FIP) of the main elements found in the solar atmosphere. Those elements with FIP values greater than 10 eV (high-FIP elements) maintain their photospheric abundances in the corona, whereas elements with lower FIP have enhanced abundances (low-FIP elements), i.e., the so-called solar/stellar FIP effect. Conversely, the inverse FIP (IFIP) effect refers to the enhancement/depletion of high-/low-FIP elements in solar and stellar coronae. FIP bias is the factor by which low-FIP elements such as Si, Mg, and Fe are enhanced or depleted in the corona relative to their photospheric abundances.

Wood & Linsky (2010) carried out a survey of FIP bias in quiescent stars with X-ray luminosities less than 10^{29} erg s^{-1}. The selection criteria excluded the most active stars. They found a clear dependence of FIP bias on spectral type in their sample of 17 G0–M5 stars. For later spectral types (G → K → M), the FIP effect observed in G-type stars, including the Sun, decreases to zero (at about K5), then becomes the IFIP effect for M dwarfs. Laming (2015), and references therein, updated and extended the sample of Wood & Linsky (2010), finding that the trend remains

the same for less active stars. When the Sun is observed as a star, i.e., observed as an unresolved point source, FIP bias is ~3–4 (for a single measurement made during solar maximum; Laming et al. 1995), similar to solar analogs χ^1 Ori (~3; Telleschi et al. 2005) and α Cen A (~4; Raassen et al. 2003). Using a long-term data series of Sun-as-a-star observations, Brooks et al. (2017) demonstrated a high correlation between the variations of coronal composition and the phase of the solar cycle using the 10.7 cm radio flux as a solar activity proxy. Recently, Doschek et al. (2015) and Doschek & Warren (2016, 2017) used spatially resolved spectroscopic observations to provide the first evidence of the IFIP effect on the Sun in the flare spectra of flaring active regions (ARs) near large sunspots. The values of solar IFIP in these specific locations are similar to the levels of IFIP observed in the M dwarf stars of Wood & Linsky (2010) and Laming (2015).

Understanding the spatial and temporal variation of elemental abundances in the solar corona provides insight into how matter and energy flow from the chromosphere into the heliosphere. The fractionation of plasma takes place in the chromosphere where high-FIP elements are mainly neutral and low-FIP elements are ionized mostly to their 1^+ or 2^+ stages. In fact, the fractionation process is likely to be related to the production of coronal plasma (Sheeley 1996). It is thought that the enhancement of low-FIP elements arises from the ponderomotive force due to Alfvénic waves acting on chromospheric ions that are preferentially accelerated into the corona while neutral elements remain behind (Laming 2004, 2009, 2012, 2015; Dahlburg et al. 2016). Ponderomotive acceleration occurs close to loop footpoints, more precisely in

the upper chromosphere, where the density gradient is steep. For the first time, Dahlburg et al. (2016) demonstrated that ponderomotive acceleration occurs at the footpoints of coronal loops as a byproduct of coronal heating in their 3D compressible MHD numerical simulations.

Solar plasma composition can be used as a tracer of the magnetic topology in the corona (Sheeley 1995) and as a means to link the solar wind to its source regions (Gloeckler & Geiss 1989; Fu et al. 2017). The magnetic field of coronal holes (CHs) extends into the solar wind and is deemed to be an open field configuration. Such fields are observed to contain unenriched photospheric plasma (Feldman et al. 1998; Brooks & Warren 2011; Baker et al. 2013), as does the fast solar wind emanating from CHs (Gloeckler & Geiss 1989). The closed field in the cores of quiescent ARs holds plasma with a FIP bias of about 3, i.e., coronal composition (Del Zanna & Mason 2014). A quiet-Sun field also has enriched plasma with a FIP bias ∼1.5–2 (e.g., Warren 1999; Baker et al. 2013; Ko et al. 2016). Blueshifted upflows located at the periphery of ARs have an enhanced FIP bias of 3–5 (e.g., Brooks & Warren 2011, 2012). These upflows may become outflows and make up a part of the slow solar wind (Brooks & Warren 2011; van Driel-Gesztelyi et al. 2012; Culhane et al. 2014; Mandrini et al. 2014; Brooks et al. 2015; Fazakerley et al. 2016).

Until recently, knowledge of FIP bias evolution was largely based on spectroheliogram observations from *Skylab* in the 1970s. In these observations, newly emerged flux is photospheric in composition (Sheeley 1995, 1996; Widing 1997; Widing & Feldman 2001). The plasma then progressively evolves to coronal FIP bias levels of ∼3 after 2 days and exceeding 7–9 after 3–7 days (Feldman & Laming 2000; Widing & Feldman 2001). Recent spectroscopic observations have revealed a different and more complex scenario for FIP bias evolution during the later stages of AR lifetimes. Baker et al. (2015) found that FIP bias in the corona decreases in a large decaying AR over 2 days as a result of the small-scale evolution in the photospheric magnetic field. Flux emergence episodes within supergranular cells modulate the AR's overall plasma composition. Only areas within the AR's high flux density core maintain coronal FIP bias. In another large decaying AR, Ko et al. (2016) also observed a decline in FIP bias over five days before reaching a basal state in the quiet Sun (FIP bias ∼1.5). This occurred as the photospheric magnetic field weakened over the same time period.

In this work, we exploit a series of spectroscopic observations to study the time evolution and distribution of plasma composition in emerging flux regions (EFRs) of varying magnetic fluxes, from ephemeral regions to pores without spots and an AR with spots. Throughout the paper, we use the term EFRs when referring to the coronal counterpart of magnetic bipoles observed in the photosphere. These regions emerge, evolve, and decay within the open magnetic field of a CH located at low solar latitude. Moreover, we use "enriched plasma" when referring to the plasma composition of FIP bias 2–3$^+$ i.e., well in excess of quiet-Sun FIP bias (∼1.5). Low-FIP elements are enhanced compared with high-FIP elements. We provide a brief description of the coronal extreme-ultraviolet (EUV) and magnetic field observations in Section 2. This is followed by a full account of the method of analysis in Section 3. Results are presented in Section 4. We discuss our results, especially within the context of the original *Skylab*

observations, in Section 5. Finally, we summarize our results and draw our conclusions in Section 6.

2. Observations

Two solar satellite observatories, the *Solar Dynamics Observatory* (*SDO*; Pesnell et al. 2012) and *Hinode* (Kosugi et al. 2007), provided the observations used in this study. *SDO*'s Atmospheric Imaging Assembly (AIA; Lemen et al. 2012) images the solar atmosphere in 10 passbands in the temperature range from 5×10^3 K to 2×10^7 K. The Helioseismic and Magnetic Imager (HMI; Scherrer et al. 2012; Schou et al. 2012) on board *SDO* makes high-resolution measurements of the line of sight and vector magnetic field of the solar surface. Both *SDO* instruments observe the full solar disk at unprecedented temporal and spatial resolutions. The Extreme-ultraviolet Imaging Spectrometer (EIS; Culhane et al. 2007) on board *Hinode* is a normal incidence spectrometer that obtains spatially resolved spectra in two wavelength bands: 170–210 Å and 250–290 Å, with a spectral resolution of 22 mÅ. Spectral lines are emitted in the EUV at temperatures ranging from 5×10^4 K to 2×10^7 K. The limited field of view of EIS is constructed by rastering the 1″ or 2″ slit in the solar west–east direction.

2.1. Coronal EUV Observations

A small CH, located in the southern hemisphere (SW quadrant), was observed by *SDO*/AIA and *SDO*/HMI beginning on 2015 November 6. For the next two solar rotations, the CH evolved and approximately doubled in area. By the time it crossed the solar central meridian on 2016 January 3, it had extended by ∼200″ into the northern hemisphere to form a narrow channel connecting to the northern polar CH. Figure 1 contains a four-panel (a–d) image of the CH from supplementary material Movie 1: (a) *SDO*/HMI magnetogram, (b) *SDO*/AIA 304 Å, (c) 171 Å, and (d) 193 Å images with the EIS field of view indicated in each panel by the white dashed box. The movie covers the period from 16:00 UT on 2016 January 4 to 23:30 on 2016 January 7. Throughout this period, the environment of the CH was highly dynamic, with repeated flux emergence, flux cancellation, jets, brightenings, and flaring.

2.2. EUV Spectroscopic Observations

Hinode/EIS tracked the CH and its surroundings from 2016 January 5 to 7, taking three successive large field-of-view rasters during the South Atlantic Anomaly-free periods on each day. Figure 2 displays the Fe XII 195.12 Å high-resolution intensity images from each raster enhanced using the Multi-scale Gaussian Normalization technique of Morgan & Druckmüller (2014). The field of view measuring 492″ × 512″ was constructed by rastering the 2″ slit in 4″ coarse steps. At each pointing position, EIS took 60 s exposures so that the total raster time exceeded two hours. The study used for these observations was specially designed for abundance measurements (Brooks et al. 2015). It contains an emission line from both a high-FIP element (S X 264.233 Å) and a low-FIP element (Si X 258.375 Å) formed at approximately the same temperature (1.5×10^6 K). To account for residual temperature and density effects on the line ratio, the study includes a series of Fe lines (VIII–XVI) covering 0.45×10^6 K to 2.8×10^6 K to determine emission measure distributions and density-sensitive
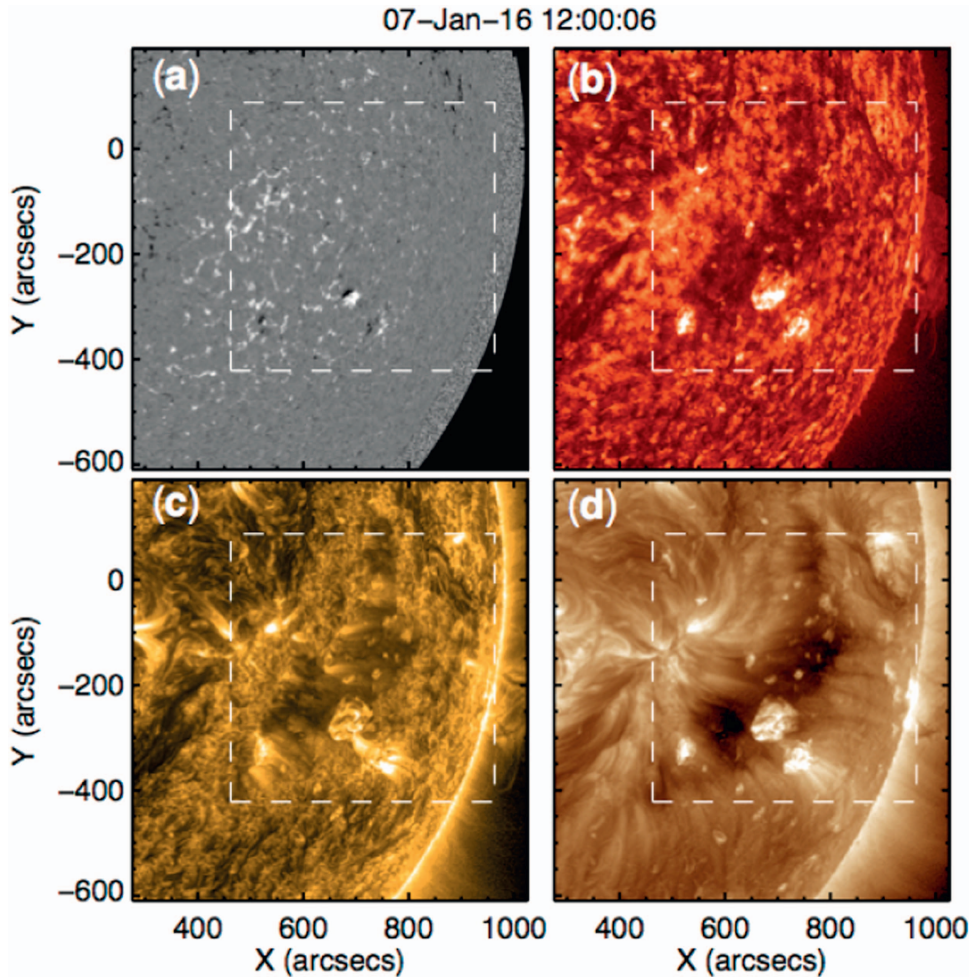
Figure 1. *SDO*/HMI line-of-sight magnetogram (a) and AIA 304 Å (b), 171 Å (c), and 193 Å (d) high-resolution images at 12:00 UT on 2016 January 7. The *Hinode*/EIS field of view is indicated by the white box. Coordinates are in arcsec (″), with the origin set at the solar disk center. High-resolution images are made using the Multi-Gaussian Normalization (MGN) technique (Morgan & Druckmüller 2014). (The figure is from Movie 1.)

(An animation of this figure is available.)

line-pair Fe XIII. The details of the *Hinode*/EIS study are given in Table 1.

2.3. Magnetic Field Observations

Figure 1(a) shows the line-of-sight magnetic field component in the *SDO*/HMI magnetogram on January 7 at 12:00 UT. The CH field was predominantly comprised of positive-polarity magnetic field. The average magnetic flux density was ∼11 G, which is typical of CHs for the declining phase of the solar cycle during which the measurements were made (Harvey et al. 1982; Hofmeister et al. 2017). A number of small bipoles emerged and/or decayed into the positive-polarity CH throughout the observing period. The range of peak flux of the bipoles extended to more than three orders of magnitude from 10^{18} Mx to greater than 10^{21} Mx. The bipoles evolved in different magnetic topological environments. Some emerged fully within the CH, so the topological environment was open, whereas other bipoles were located along the CH boundary so that one polarity was in close proximity to an open magnetic field and the opposite polarity was near a closed field. Three of the largest EFRs are close to the southern edge of the *Hinode*/EIS field of view in Figure 1.

3. Method of Analysis

3.1. Region Definition

We identified seven EFRs in the CH and along its boundary with the quiet Sun. In Figure 2, they are labeled R1–R7 in descending order of maximum magnetic flux. Defining and tracking these regions in the *Hinode*/EIS observations required great care, as their average FIP bias values were sensitive to the extent of, and features contained within, the selected areas. To minimize the effect of non-EFR pixels, individual regions were extracted from each raster image using a histogram-based intensity thresholding technique similar to the one employed by Krista & Gallagher (2009). Intensity thresholding provides a quantitative method for identifying the main features within each of the nine rasters. We were able to distinguish CH and quiet-Sun pixels from EFR pixels within the selected area using this method.

A histogram of EFR R3 Fe XII 195.12 Å intensity at 14:46 UT on January 6 is shown in Figure 3 as an example. The trimodal distribution corresponds to the CH, quiet Sun, and EFR within the image of the area surrounding R3 (see the reverse color image in the left panel of the inset in Figure 3). The first two modes of the histogram, with intensity peaks at ∼150 and ∼320, are associated with the CH and quiet Sun portions of the
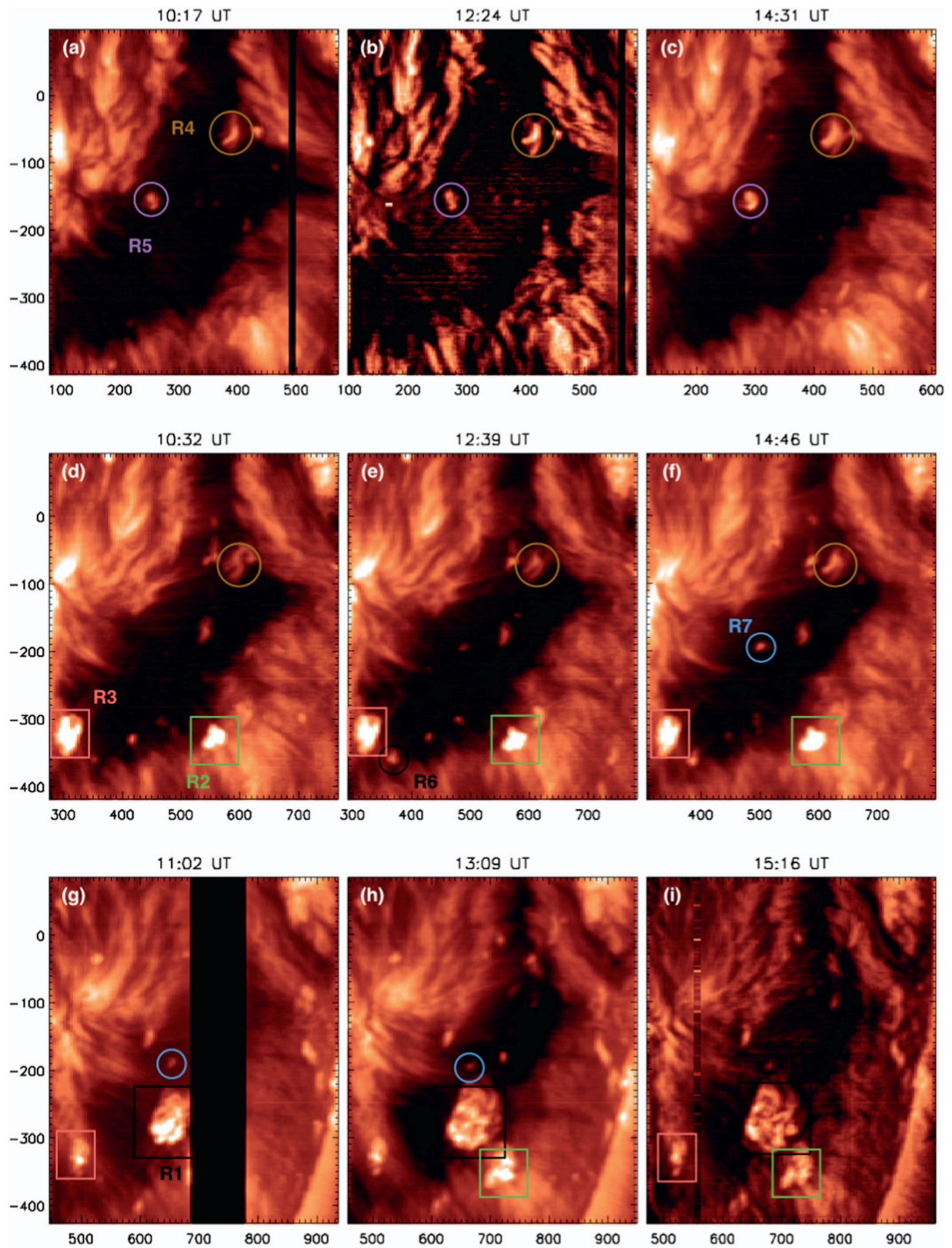
Figure 2. *Hinode*/EIS Fe XII 195.12 Å intensity maps for 5 (top), 6 (middle), and 7 (bottom) 2016 January. Regions R1–R7 in the text and Table 2 are encircled/surrounded in the EIS maps for which FIP measurements are made (colors correspond to Figure 6: R1—black box, R2—green box, R3—red box, R4—tan circle, R5—purple circle, R6—black circle, R7—blue circle). Coordinates are in arcsec (″), with the origin at the solar disk center. Images are enhanced using the Multi-scale Gaussian Normalization technique (MGN; Morgan & Druckmüller 2014). Figure 8 contains a zoomed-in intensity map that corresponds to R1 and R2 in panel (h).

Table 1
Hinode/EIS Study Details

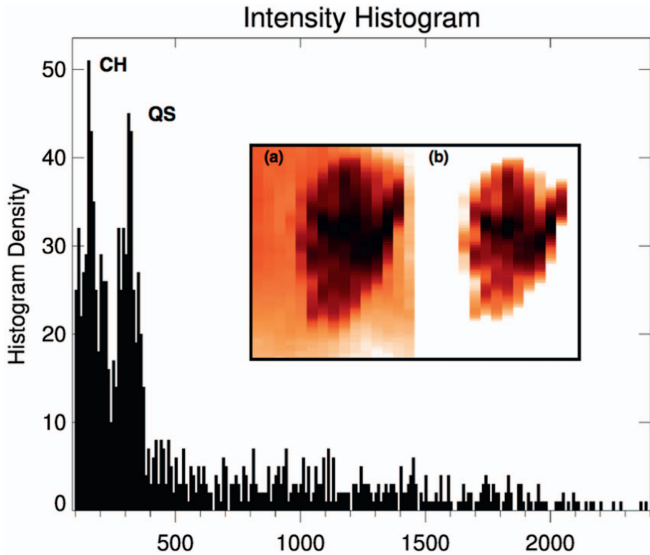|	
Study number	513
Emission Lines	Fe VIII 185.213 Å, Fe IX 188.497 Å
	Fe X 184.536 Å, Fe XI 188.216 Å
	Fe XI 188.299 Å, Fe XII 192.394 Å
	Fe XII 195.119 Å, Fe XIII 202.044 Å
	Fe XIII 203.826 Å, Fe XIV 264.787 Å
	Fe XV 284.16 Å, Fe XVI 262.984 Å
	Si X 258.375 Å, S X 264.233 Å
Field of view	$492'' \times 512''$
Rastering	$2''$ slit, 123 positions, $4''$ coarse steps
Exposure Time	60 s
Total Raster Time	2 hr 7 min

Figure 3. Histogram of Fe XII intensity in erg cm^{-2} s^{-1} sr^{-1} within the submap of EFR R3 (left panel of the inset). Coronal hole (CH) and quiet Sun (QS) intensity peaks are indicated. The local minimum after the quiet-Sun peak at 400 is the intensity threshold, below which pixels are masked from the region. FIP measurements are determined by averaging spectra of the unmasked pixels with intensities greater than 400 (right panel of the inset). Unmasked (a) and masked (b) intensity maps are displayed in reverse colors so that EFR features are dark and the surrounding CH is light.

distribution, respectively. The local minimum at ∼400 occurring after the second peak was used to establish the cutoff threshold intensity level for EFR R3 in this raster. Pixels with values below the cutoff were masked from the region. The unmasked (a) and masked (b) quiet-Sun and CH pixels/areas are shown in the inset of Figure 3. EFR R3 was located at the edge of the CH (middle and bottom rows of Figure 2), close to the nearby quiet Sun, so a trimodal intensity distribution is expected. For EFRs located entirely within the CH, the intensity histogram was bimodal, one mode each for the CH and EFR pixels. The cut-off threshold was then the local minimum after the CH peak in the intensity distribution. The intensity thresholds used to identify CH, quiet Sun, and EFR for R1–R7 varied by ∼20%, depending on whether the EFR was fully surrounded by a CH or a mix of a CH and quiet Sun. A number of EFRs were excluded from the study because they contained too few EFR intensity pixels (<50), e.g., R7 in Figures 2(e) and (i) and R6 in Figure 2(f).

The effect of instrumental stray light is estimated to be ∼2% of the typical counts for Fe XII observations of the quiet Sun (see *Hinode*/EIS Software Note No. 12). For CH observations, the effect is likely to be slightly higher. Based on the intensity histogram in Figure 3, the threshold for CH pixels is 150 erg cm^{-2} s^{-1} sr^{-1}, compared to 400 erg cm^{-2} s^{-1} sr^{-1} for quiet-Sun pixels, therefore we estimate the stray light effect to be 4%–5%. In the case of the Si X–S X FIP bias ratio, the effect is present in both lines, therefore we would expect a differential effect that is lower than that for a single ion. Moreover, the overall effect of stray light on the FIP bias measurements will be negligible, since we are removing CH pixels and using only EFR pixels from the masking process.

3.2. FIP Bias Measurements

Hinode/EIS data reduction was carried out using standard routines that are available in Solar SoftWare (Freeland & Handy 1998). The eis_prep routine converts the CCD signal in each pixel into calibrated intensity units and removes/flags cosmic rays, dark current, dusty, warm, and hot pixels. All data were corrected for instrumental effects as follows. The orbital spectrum drift and CCD spatial offsets were corrected using the artificial neural network model of Kamio et al. (2010). The grating tilt was adjusted using the eis_ccd_offset routine. Finally, the CCD detector sensitivity was corrected using the method of Del Zanna (2013), which assumes no degradation after 2012 September.

All spectral lines from consecutive ionization stages of Fe VIII–XVI were fitted with single Gaussian functions, with the exception of the known blends of the Fe XI, XII, XIII lines for which multiple Gaussian functions were necessary to distinguish the blended lines. Single Gaussian functions were also fitted to the Si X and S X lines used to determine FIP bias. This ratio shows some sensitivity to temperature and density, but our method is designed to remove these effects and the diagnostic has been proven to be robust in the composition analysis of a variety of features (see references in the introduction and Brooks & Warren (2011) for a detailed discussion).

The density was measured using the Fe XIII line-pair diagnostic ratio. The Fe XIII ratio is highly sensitive to changes in density (Young et al. 2007) and both lines are located in the 185–205 Å wavelength range, where the EIS instrument is most sensitive. These factors combine to make the Fe XIII ratio the best EIS coronal density diagnostic (Young et al. 2007), however, its formation temperature is ∼0.4 MK higher than that of Si X and S X lines used in this study. The difference in formation temperatures raises the possibility that Fe XIII may be sampling different plasma from that of the Si X and S X emitting plasma. Young et al. (2009) conducted high-precision density measurements using Fe XII and Fe XIII line pairs and found that the two different density diagnostics showed broadly the same trend in density across ARs. They concluded that any discrepancies in densities are most likely due to the atomic data for the ions, rather than any real physical differences in the emitting plasmas. Subsequently, Fe XII atomic data have been updated and improved by Del Zanna & Storey (2012) so that now the densities are in agreement for the two ions (FeXII and Fe XIII). These results provide solid evidence that the *Hinode*/EIS is likely to be sampling the same plasmas, since Si X, S X, and Fe XII have the same formation temperature of 1.6 MK.

The CHIANTI Atomic Database, Version 8.0 (Dere et al. 1997; Del Zanna et al. 2015), was then used to carry out the calculations of the contribution functions, adopting the photospheric abundances of Grevesse et al. (2007) for all of the spectral lines, while assuming the previously measured densities. The emission measure distributions were computed

from the Fe lines using the Markov-Chain Monte Carlo (MCMC) algorithm available in the PINTofALE software package (Kashyap & Drake 2000) and then convolved with the contribution functions and fitted to the observed intensities of the spectral lines from the low-FIP element Fe. As Si is also a low-FIP element, the emission measure was scaled to reproduce the Si X line intensity. FIP bias was then the ratio of the predicted to observed intensity for the high-FIP S X line. If the emission measure scaling factor of the Si X line intensity derived from the Monte Carlo simulations to fit the observed line intensity was larger than the approximately 22% intensity calibration uncertainty, then the pixels were excluded from consideration in our study, e.g., R3 in Figure 2(h) and R6 in Figure 2(f) (Lang et al. 2006). The scaling factor helps to account for any absolute calibration errors between the long wave and short wave detectors of *Hinode*/EIS. A full account of the method is available in Brooks et al. (2015).

To determine the mean FIP bias values within EFR R1–R7, profiles for each spectral line were averaged across all of the EFR pixels that were identified by the histogram-based intensity threshold technique in Figure 3. Although spatial information was lost when the profiles were averaged, the signal-to-noise was enhanced. This is a necessary tradeoff when measuring intensities within low-emission regions such as EFRs in CHs. The averaged profiles were fitted with single or multiple Gaussian functions and then the steps described above were carried out. For the spatially resolved composition map in Section 4.2, the method was also applied to each pixel within the map; therefore, no averaging was performed. In this way, we retained the details of the FIP bias distributions within the larger EFRs (R1, R2).

Uncertainties in the FIP bias measurements are difficult to quantify because errors in the atomic data and radiometric calibration are likely to be systematic in nature. We conducted a series of experiments where intensities for a sample spectrum were randomly perturbed within the calibration error, and the standard deviation from a distribution of 1000 Monte Carlo simulations was calculated for a single pixel. These experiments produced an uncertainty of $\sim$0.3 in the absolute FIP bias for single pixels within the composition map.

When the intensities of N pixels are summed the statistical error is expected to be reduced by a factor of $1/\sqrt{N}$ for random fluctuations. The mean FIP bias values of EFR R1–R7 were calculated over a range of $N = [50, 2154]$, therefore the corresponding reduced uncertainties were in the range [0.04, 0.006] in mean FIP bias. Moreover, we investigated how FIP bias varied from one measurement to the next using a series of sit and stare observations of an AR where *Hinode*/EIS is operating in the fixed target mode rather than rastering mode. During sit and stare observations, the slit is pointed at a feature on the Sun and a series of exposures is taken as the spacecraft tracks that feature. Four sit and stare rasters from 2015 October 24 at 01:35, 02:32, 03:29, and 04:25 UT were used to conduct the test. (For EIS Study 519 details, please see http://solarb.mssl.ucl.ac.uk/SolarB/ShowEisStudy.jsp). These observations provide a measure of how FIP bias changed with time over a period of $\sim$3.7 hr (each exposure lasted for 60 s and the total number of exposures was 220). The mean variation per pixel was 0.07. The test shows that the uncertainties due to random fluctuations and variations from exposure to exposure are probably below 0.1 for the relative abundance measurement per pixel. For the mean FIP bias of an EFR, following the above

argument, the statistical error is expected to be much lower than 0.1. We still use this conservative error estimation in Figure 6 because FIP bias measurements are highly complex.

3.3. Magnetic Field Measurements

A series of *SDO*/HMI line-of-sight magnetograms was used to determine emergence times, peak magnetic flux, magnetic flux density, and estimates of loop length for the bipoles. The studied time period was from 00:00 UT on 2016 January 2 to 00:00 UT on 2016 January 8 using magnetograms at a cadence of 30 minutes. An automated procedure, adapted from the method of James et al. (2017), was used to measure the magnetic flux associated with the regions of the emerging bipoles. Contours were drawn at $\pm$30 G on each line-of-sight magnetogram so that only pixels with magnetic flux densities greater than 30 G in magnitude were considered, and a further area threshold of 10 pixels was set so that only locations within contours that contained 10 or more pixels were used. These criteria combined to exclude weak field, as well as small patches of pixels dominated by noise. The total magnetic flux within the contours that satisfied both threshold criteria was then calculated for each magnetogram for each bipole region. Only the negative polarity was used for measurements of magnetic flux because the bipoles emerged in a positive-polarity CH, making it difficult to separate the positive flux associated with the emerging bipoles from the background CH field.

Values of magnetic flux density and estimated bipole loop length were determined at the times that FIP measurements were made. Loop length estimates were made by taking the flux-weighted centers of the positive and negative parts of the bipoles, then using the separation of the centroids to calculate the lengths of semi-circular loops. For EFRs R3–R5 and R7, *SDO*/AIA 193 Å images overlaid with *SDO*/HMI magnetic field contours were used to identify different loop connectivities within the EFRs (see an example of R3 in Figure 4). Distances between the negative and positive centroids for each set of loops were determined. Because the positive flux had to be considered for the loop length estimates, the bipoles were isolated from any background CH field. This was done for both polarities using the magnetograms closest to the times of the FIP bias measurements. Only the contours that were determined by eye to enclose flux that corresponds to the desired bipole emergence were selected. Magnetic flux densities were also calculated for the negative polarity using these selected contours near the FIP measurement times by summing the magnetic flux density values within the selected contour and dividing by the total area within the contour.

4. Results

4.1. Evolution of Mean FIP Bias in EFRs R1–R7

Our results are tabulated in Table 2, where we show the mean FIP bias, hours from emergence in HMI magnetograms (called "age"), peak flux, and emergence/decay phases for EFRs R1–R7. Peak negative flux ranged from 1.3×10^{19} (R7) to 3.8×10^{21} Mx (R1). The EFRs are classified as ephemeral regions, R4–R7, small ARs without spots, R2–R3, and an AR with spots designated AR 12481, R1 (cf. van Driel-Gesztelyi & Green 2015). With the exception of R1, the largest region, all EFRs had short lifetimes of 1–4 days and emergence/rise phases lasting for 0.25–3.5 days. R1 emerged two days before
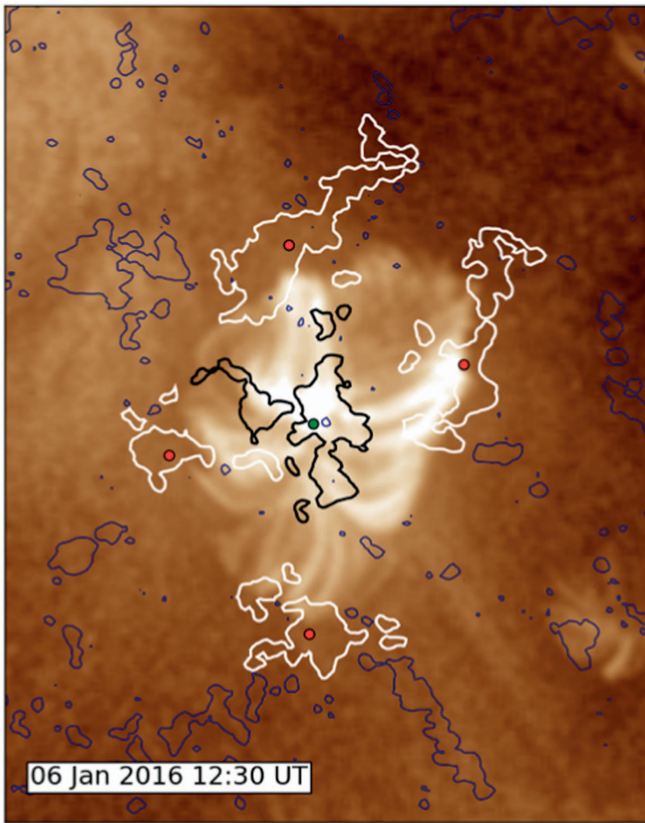
Figure 4. *SDO*/AIA 193 Å high-resolution image overlaid with the *SDO*/AIA magnetic field contours (positive/negative ±30 G) of EFR R3. Four groups of loops connecting the negative polarity with four separate positive polarities are identified. Flux-weighted centroids of both polarities are indicated by the dots (green/red are negative/positive centroids). Loop lengths were then determined for each set of loops using the distance between the centroids.

Table 2
EFR Characteristics

Region (lifetime)	FIP Bias	Hours from Emergence	Peak Flux (10^{19} Mx)	Phase
1 (NA)	1.8	16.5	⋯	Emergence (E)
	1.8	18.7	⋯	Emergence (E)
	1.9	20.8	<-380	Emergence (E)
2 (NA)	1.5	23.0	⋯	Emergence (M)
	1.7	25.2	⋯	Emergence (M)
	1.7	27.3	-16	Emergence (M)
	1.8	49.7	⋯	Decay (M)
	1.8	51.8	⋯	Decay (M)
3 (NA)	1.8	18.5	-15	Decay (E)
	1.9	20.7	⋯	Decay (E)
	1.8	22.8	⋯	Decay (E)
	1.7	43.0	⋯	Decay (L)
	1.2	47.3	⋯	Decay (L)
4 (83 hr)	2.0	52.8	-8.4	Decay (L)
	1.8	54.9	⋯	Decay (L)
	1.9	57.0	⋯	Decay (L)
	1.9	77.0	⋯	Decay (L)
	1.7	79.2	⋯	Decay (L)
	1.5	81.3	⋯	Decay (L)
5 (31 hr)	1.7	16.3	-3.1	Decay (E)
	2.1	18.4	⋯	Decay (E)
	2.5	20.5	⋯	Decay (E)
6 (33 hr)	1.2	3.5	-2.1	Emergence (L)
7 (22 hr)	1.7	11.3	-1.3	Emergence (L)
	2.0	33.7	⋯	Decay (L)
	1.6	35.8	⋯	Decay (L)

Note. Lifetime, mean FIP bias measurements for Regions R1–R7 (ranked by peak flux), time from emergence in hours, peak negative flux values for each flux region, and phase of flux region's life cycle. In the first column, estimated lifetimes of R4–R7 are provided in brackets after the region numbers. R1–R3 rotated over the limb after their peak flux but before they dispersed into the background field, therefore their lifetimes cannot be estimated. Estimated uncertainty in mean FIP bias is <0.1 (see Section 3.2). Time from emergence was calculated from when the regions emerged in HMI magnetograms until they were observed in *Hinode*/EIS rasters. The peak flux of R1 is given as of 00:00 UT on January 8, but the true peak occurred after the EFR rotated over the west limb. Emergence/decay phase is before/after peak flux. (E), (M), and (L) refer to early, middle, and late, respectively, for emerging or decay phases.

it rotated over the western limb, therefore we were unable to determine its peak flux or lifetime. The normalized flux profile of R2 in Figure 5 shows some of the typical characteristics of flux evolution in small regions. The emergence/decay phases are of nearly comparable duration, an important difference compared to ARs where the decay phase is much longer than the emergence phase.

The lowest mean FIP bias of 1.2 (i.e., nearly photospheric composition) occurred in R6, 3.5 hr after it emerged in the CH and in R3 during the late-decay phase, two days after emergence. EFR R5 had the highest value of 2.5, which is indicative of enriched plasma (compared to a quiet-Sun FIP of ∼1.5), and it was measured during the decay phase ∼20.5 hr after emergence. We observed three other EFRs (R1, R2, and R7) during their emergence phases and all had enhanced mean FIP biases, >1.5 at 11–27 hr after emergence, assuming photospheric composition (FIP bias of 1) at the time of emergence. In general, mean FIP bias was enhanced to levels greater than that of the quiet Sun (FIP bias of ∼1.5) less than a day from the beginning of flux emergence in HMI magnetograms.

Hinode/EIS observed the evolution of mean FIP bias in six of the seven EFRs for periods lasting from a few hours to two days. Figure 6(a) shows mean FIP bias versus time from emergence (age). The values in the plots are from Table 2 and were determined using an average of N pixels within each region. Therefore, the uncertainty is estimated to be <0.1 in

mean FIP bias (see Section 3.2). Filled/unfilled symbols denote the emergence/decay phases of the EFRs (cf. Table 2). Three EFRs (R3, R4, and R7) had similar patterns of mean FIP bias evolution during the EIS observing period. They maintained steady plasma composition for approximately one day before declining to levels that are more typical of either the quiet Sun (∼1.5 for R4 and R7), the so-called basal state (Ko et al. 2016), or photospheric FIP bias levels of the surrounding CH (R3). Next, EFR R2 had increasing mean FIP bias for a day; however, we are unable to comment on later evolution because *Hinode*/EIS no longer observed the CH after the last raster at 15:15 UT on January 7.

EFR R5 exhibited anomalous mean FIP bias evolution in comparison to the other regions. In the first observation, R5 appeared to have reached an enriched plasma composition on a similar timescale as all other regions; however, R4 was not observed early enough to draw any conclusions. Mean FIP bias
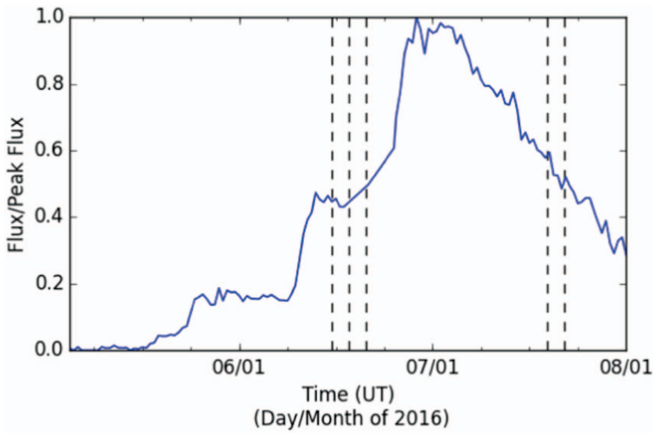
Figure 5. Plot of the total negative magnetic flux normalized to peak flux vs. time. The dashed vertical lines indicate the times of FIP measurements for R2 (See Table 2). The comparable length of the emergence and decay phases is typical of smaller EFRs.

then rapidly increased from 1.7 to 2.5 in 4.2 hr to reach the highest level in our study. The plasma is enhanced at a rate of $0.2\ h^{-1}$ in mean FIP bias. In contrast, mean FIP bias increased by an order of magnitude slower in the range of $[0.03, 0.06]\ h^{-1}$ for R1–R3, and R7 (based on the change from photospheric FIP bias of 1 at the first magnetic appearance up to the emergence/early-decay phase of each region). Finally, mean FIP bias decreased by ~0.1–$0.2\ h^{-1}$ in R3, R4, and R7 (based on the sharp decrease in mean FIP bias for the last 2–3 measurements).

There was no real change in the mean coronal composition of R1 since it was observed for a short time interval. Mean FIP bias was 1.8–1.9 for 4.3 hr on January 7. This region was the largest in our sample and was in the very beginning of its emergence phase, unlike the other regions, which were observed from the late stages of emergence to late-decay phases.

We investigated mean FIP bias parameter space and found no apparent trends in mean FIP bias versus peak magnetic flux, normalized peak magnetic flux, or emergence time, i.e., the time period from the beginning of emergence to peak flux. Next, we tested the possible dependence of the mean FIP bias on two parameters, loop length and magnetic flux density. Figure 6(b) shows mean FIP bias versus loop length (Mm). For EFRs with multiple loop connectivities, the plotted loop length is an average value of loops within the EFR at the time of the mean FIP bias measurements. The number of loop groups per region ranged from 2–5, with variances in the loop length as small as ±5 Mm for R4 and as large as ±19 Mm for R5. In our sample and within the estimated uncertainties, there is no FIP bias dependence with loop length. Mean FIP bias versus magnetic flux density is displayed in Figure 6(c). Overall, the graph shows a decreasing trend in mean FIP bias with increasing flux density (with the exception of R1; see the inset in Figure 6(c), where values are too close to derive a reliable trend).

4.2. Plasma Composition Map

Typically, the emergence of a bipole within a CH leads to the formation of an "anemone" structure in the corona; see Figures 7(a) and (b). The emerging flux interacts with the surrounding CH field via interchange reconnection of
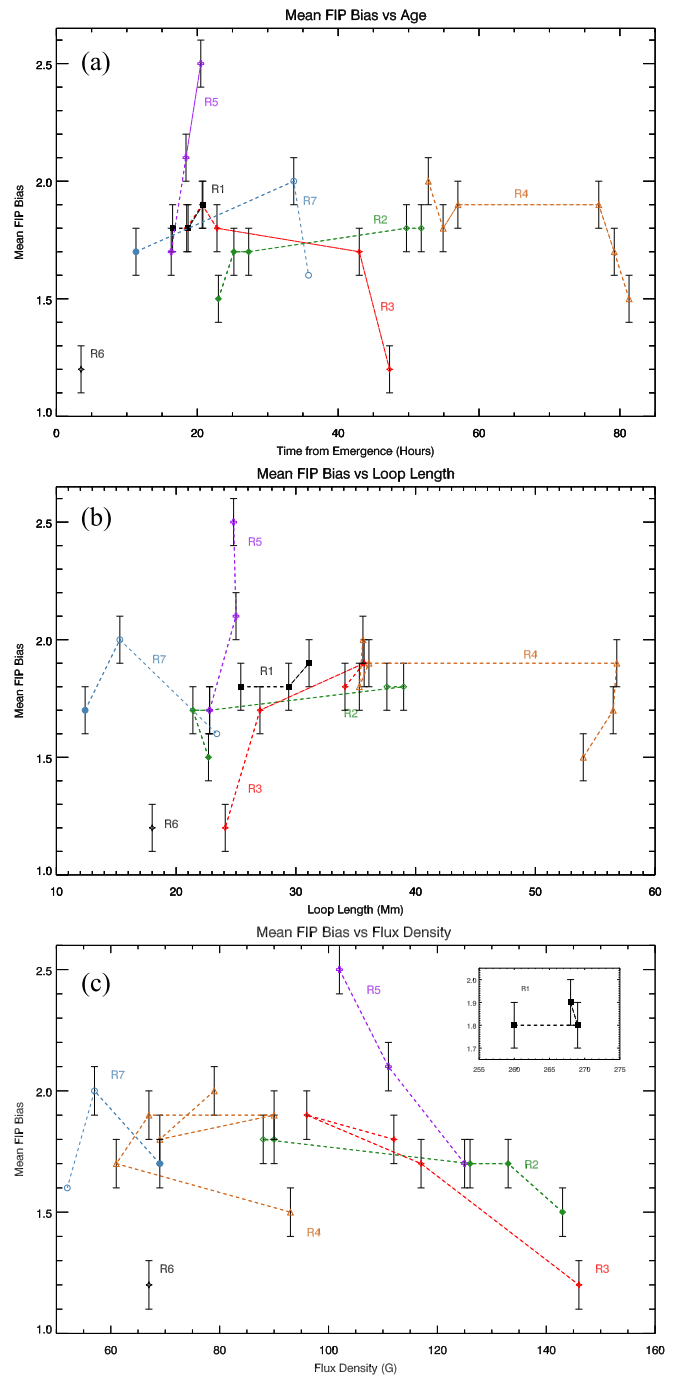

Figure 6. (a) Mean FIP bias vs. time from emergence (i.e., age), (b) mean FIP bias vs. loop length (Mm), and (c) mean FIP bias vs. magnetic flux density. Filled/open symbols represent times of mean FIP bias measurements prior to/after peak magnetic flux. R1–R7 refer to regions labeled in Figure 2. The inset in (c) shows R1 separately to improve the display of the other regions. Uncertainty is <0.1 in mean FIP bias (see Section 3.2).

oppositely directed field. New loops extend radially from the location of the included EFR polarity. Movie 2 shows the three largest regions R1, R2, and R3, evolving into classic anemone regions in the $SDO/$AIA 171 and 193 Å passbands.

EFR R1 emerged in the open magnetic field environment of the CH 33 hr after EFR 2, which emerged at the boundary between the CH and quiet Sun. The natural expansion of the growing EFRs leads to new, extended loops forming at the
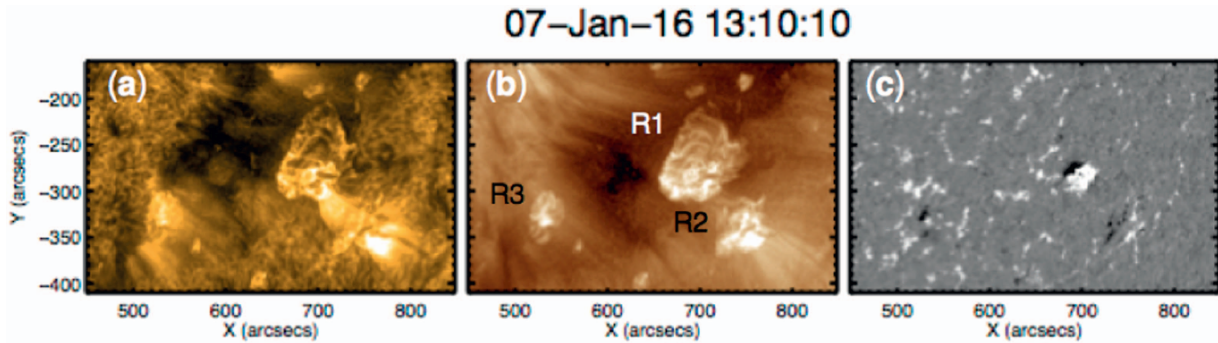
Figure 7. *SDO*/AIA 171 Å (a) and 193 Å (b) images, and *SDO*/HMI magnetogram (c) of EFRs R1, R2, and R3 at 13:10 UT on January 7. Images are taken from Movie 2.

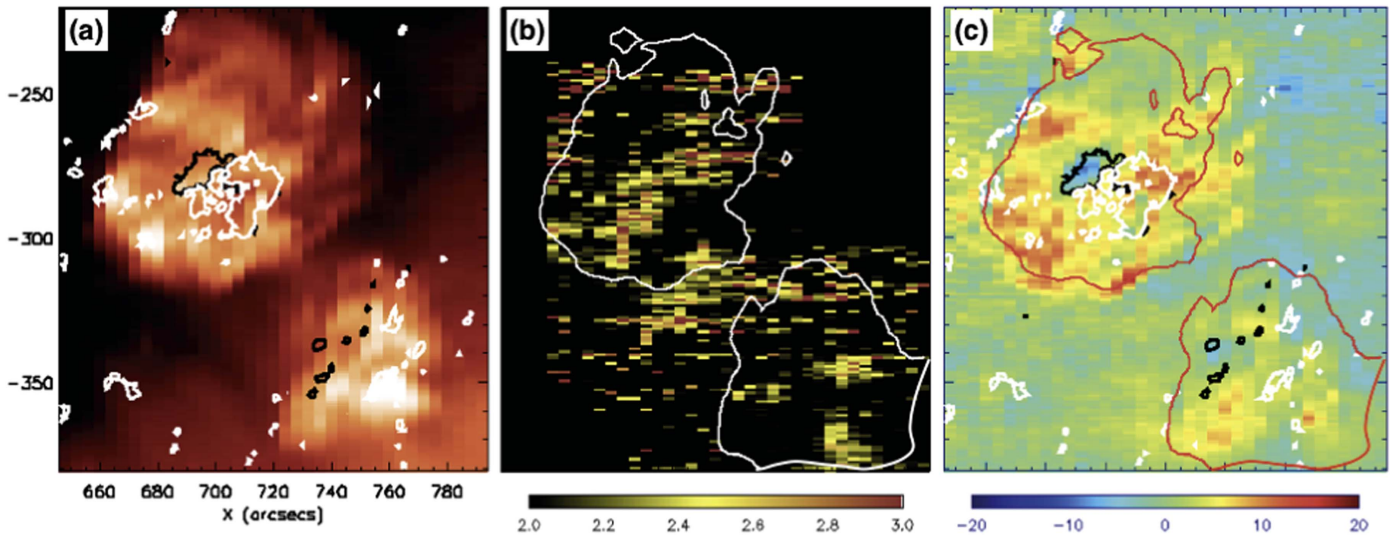(An animation of this figure is available.)

Figure 8. (a) *Hinode*/EIS Fe XII 195 Å intensity map overlaid with ±100 G magnetic flux contours. (b) A composition map showing only FIP bias values greater than 2 overlaid with the contours of the masks determined using the intensity threshold method (see Section 3.1). (c) A Fe XII 195 Å Doppler velocity map overlaid with magnetic flux and mask contours. Regions 1 and 2 are timestamped at 13:09 on January 7. The estimated uncertainties within the composition map are ±0.3 per pixel (see Section 3.2).

interface of the two regions where the magnetic field was oppositely aligned. Movie 2 and Figures 7(a), (b) show the coronal interconnectivity of the EFRs. Figure 8 displays *Hinode*/EIS zoomed-in Fe XII intensity and Doppler velocity maps and a Si X–S X composition map for R1 and R2 on January 7 (cf. Figure 2(h)). The CH appears dark in the intensity map, whereas the EFRs are bright, compact features. The corresponding locations in the Doppler velocity map show plasma flows almost at rest with isolated patches of blueshifted plasma flows of 10–20 km s^{-1} along the open field of the CH, and redshifted plasma flows of 10–20 km s^{-1} contained within the closed loops of the EFRs. These are typical velocity ranges for CHs and quiescent ARs.

The composition map shows FIP bias values greater than 2 so that locations of enriched FIP bias are clearly visible within the two EFRs. CH and quiet-Sun pixels have FIP bias <2. The contours of the masks described in Section 3.1 are overlaid on the composition and Doppler velocity maps. Within the contours, some of the bright loops contain plasma enriched well above a quiet-Sun FIP bias of ∼1.5. Moreover, where the EFRs connect with each other (R1 and R2), FIP bias is once again enriched.

Figure 9 shows the relative frequency distributions of FIP bias within the mask contours for EFRs R1 and R2. The distributions are skewed to higher FIP bias values and the percentages of pixels of FIP bias greater than 2 are 36% and 32%, respectively. The spatially resolved composition map and the frequency distributions clearly show that FIP bias varies from photospheric up to coronal values across EFRs of different sizes.

5. Discussion

5.1. Comparison of EFRs and ARs

The EFRs in our study are at the small end of the size-spectrum of ARs (van Driel-Gesztelyi & Green 2015). Only the stronger magnetic fields of the largest EFRs, R1–R3, are organized according to Hale's polarity law. The smaller regions, R4–R7, have anti-Hale orientations with a large scatter of inclination angles, as they are presumably too small to resist the buffeting effects of convection (Longcope & Fisher 1996).

The small magnetic flux content of EFRs has implications for the ratio of the length of the emergence phase to the lifetime of the AR. Harvey (1993) and van Driel-Gesztelyi & Green (2015)
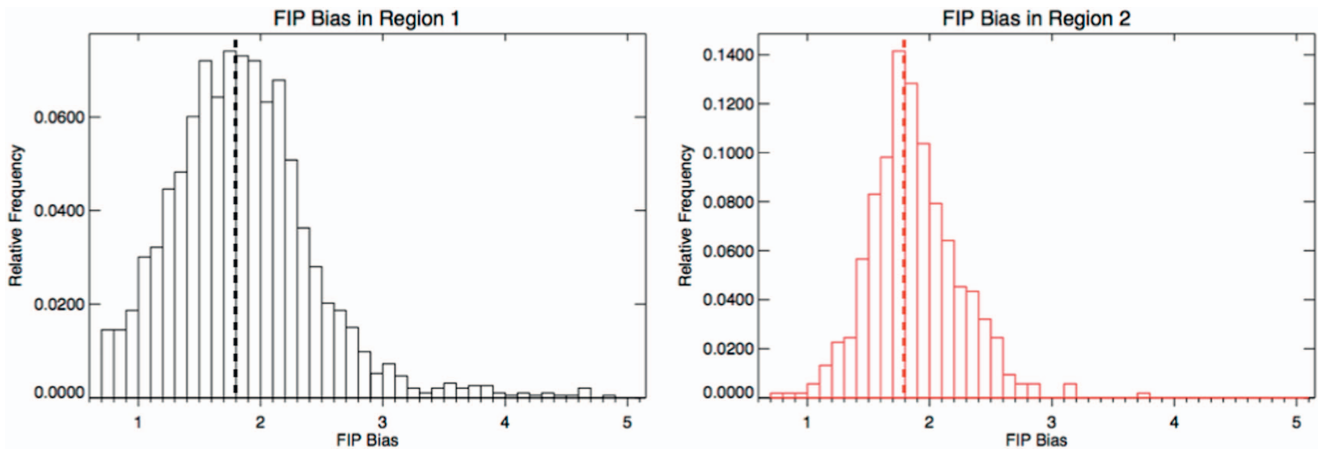
Figure 9. Histograms of FIP bias in regions R1 and R2 defined with intensity thresholds and shown in the composition map in Figure 8. The dashed lines correspond to mean FIP bias values.

show that for EFRs comparable to the ones in our study, the duration of the emergence phase is ∼30% of the lifetime. For full-sized ARs, the percentage goes down to <15%. As AR size decreases, the asymmetry of the emergence and decay phases also decreases so that the ephemeral-like EFRs are close to having the emergence and decay phases of comparable time periods (cf. Figure 5).

5.2. Emergence/Early-decay Phase

Skylab spectroheliogram observations showed that the average composition of ARs is photospheric just after emergence (e.g., Sheeley 1995, 1996). There is a progressive enrichment of the plasma at an almost constant rate in the evolving regions so that within two days, the plasma is modified to a mean FIP bias ∼3–4 and after a week, it exceeds 7 (Widing & Feldman 2001). In the observations shown here, the plasma composition in five of seven EFRs within the CH had evolved to levels exceeding quiet-Sun values (>1.5) in less than a day after emergence (see Table 2 and Figure 6).

Based on the length of the emergence phases of the four ARs in the *Skylab* study (2–5 days), we estimate that their maximum magnetic fluxes range from 5×10^{21} to 10^{22} Mx (van Driel-Gesztelyi & Green 2015). They would be classified as large ARs with lifetimes of weeks to months. Here, the EFRs were much smaller by as much as 1–2 orders of magnitude, with the exception of R1 (3.8×10^{21} Mx), so their lifetimes were measured in days.

As ARs, EFRs are presently understood to be the product of the amplification of the magnetic field in a sub-photospheric dynamo (Cheung & Isobe 2014). Both magnetic buoyancy and upward convective motions participate in the transport of the magnetic field toward the photosphere, then its emergence through the photosphere before it rises into the chromosphere and then into the corona. Because of the formation process, the plasma of the emerging flux tube at the photospheric level is expected to have (sub-) photospheric composition, while the modification of this composition at the coronal level typically takes a day (see references in Section 1). Based on the early observational results from *Skylab* (Sheeley 1995, 1996; Widing 1997; Widing & Feldman 2001) and the current understanding of flux emergence theory (Cheung & Isobe 2014), the assumption that the plasma has photospheric composition at the time of emergence is reasonable.

In the four ARs observed by *Skylab*, the mean FIP bias ratio increases at a rate of approximately [0.04, 0.1] h^{-1} and is maintained for 5–7 days during their emergence phases. Four flux regions in our study exhibited comparable positive rates of enrichment [0.03, 0.06] h^{-1} during their emergence/early-decay phases. The rates of enrichment determined from our observations are based on the assumption that the EFRs emerged with FIP bias of 1 (i.e., the plasma was unfractionated at the time the EFRs are identified in the photospheric magnetograms of HMI, as observed for R6, Figure 6(a)) and then increased linearly for ≲1 day until the time of the first FIP bias measurements (cf. Table 2). The linear trend in the evolution of plasma composition from emergence to peak flux/early-decay phase assumed here is likely to be an oversimplification. These are short-lived, relatively small flux regions that are located in a complex environment within or nearby a CH. Further *Hinode*/EIS observations are needed to test the FIP bias values at the beginning of the emergence phase.

Any discussion of FIP bias evolution is complicated by the fact that S has a FIP of 10.36 eV and thus lies on the boundary between low and high-FIP elements. Observations have shown that S behaves like a high-FIP element in ARs (Lanzafame et al. 2002), whereas it is more like an "intermediate" FIP element in the quiet Sun (Brooks et al. 2009), i.e., S fractionates more than other high-FIP elements, which is consistent with some model predictions (e.g., Laming 2012). Notwithstanding the "hybrid" nature of S, the Si X–S X FIP bias diagnostic does behave as would be expected from a low-/high-FIP bias ratio. In this study and in previous work, FIP bias is 1 in the CH (masked from the spatially resolved map in Figure 8), and quiet-Sun FIP bias is 1.5–2 and ⩾3 for ARs (cf. references in Section 1). The Si X–S X FIP bias ratio can distinguish between different levels of fractionation even if S is not behaving fully like a high-FIP element, as shown in previous studies and by the time evolution of the EFRs in Figure 6. In summary, the fractionation may be understated compared to what would be measured using a different FIP bias diagnostic ratio such as Fe/O.

5.3. Late-decay Phase

For those EFRs where we have sufficient measurements over time, mean FIP bias decreased during the late-decay phase for a further 1–2 days, while the magnetic field of the EFRs was

dispersing. The processes in the decay phase involve the interaction between supergranular cells and the dispersing magnetic flux. The convection-buffeted flux concentrations become confined to intergranular lanes, outlining the ever-evolving supergranular cells. Along the supergranular boundary lanes, opposite-polarity flux concentrations meet and cancel, a process that effectively and quickly removes the minority-polarity flux of these EFRs (i.e., negative polarity in this CH).

In a large AR, Baker et al. (2015) demonstrate that AR plasma with mean FIP bias $\sim$3 may be modulated by small bipoles emerging at the periphery of supergranular cells containing photospheric material reconnecting with the pre-existing AR field. A similar scenario is likely to affect the observed mean FIP bias levels in the smaller EFRs, as the decay processes are not unique to large ARs, in particular interaction and plasma mixing with surrounding fields. Furthermore, Ko et al. (2016) show a temporal evolution from moderate to strong positive correlation of FIP bias and the weakening photospheric magnetic field strength during the decay phase of a large AR, with the largest decrease in FIP bias occurring in plasma at $\sim$2 MK. Once the photospheric magnetic field evolves to below 35 G, FIP bias in the AR reaches a quiet-Sun basal state for FIP bias $\sim$1.5. The correlation of FIP bias and magnetic field strength in their study does not hold below 10 G, which is a typical mean field strength for CHs.

In our study, the rates of change in mean FIP bias in the small flux regions during their late-decay phase are significantly faster than the rates of change observed in larger decaying ARs. Baker et al. (2015) and Ko et al. (2016) find remarkably similar rates of decreasing mean FIP bias in the range [0.004, 0.009] h^{-1} within the core of ARs over 2–5 days compared to a range of [0.1, 0.2] h^{-1} for R3, R4, and R7 during their late-decay phase. Once again, the rates of decrease exhibited in the large ARs are maintained over periods of days, whereas in the small regions within the CH, the rapid changes occurred in a matter of hours.

5.4. Spatial Distribution of FIP Bias

The spatially resolved composition map in Figure 8, as well as maps in previous studies (e.g., Baker et al. 2013, 2015; Brooks et al. 2015), have revealed that FIP bias does vary over spatial scales of a few arcseconds. Patches of higher FIP bias ($>$2) were found in the core of the EFRs, which is consistent with the *Hinode*/EIS observations of large ARs in Baker et al. (2013, 2015).

There was enriched plasma in the vicinity of loops linking the positive polarity of R1 and the negative polarity of R2 (see patches of FIP bias in the range [2, 3] between the mask contours of Figure 8(b), which spatially correspond to the loops connecting R1 and R2 in Figures 7(a), (b) and Movie 2). The magnetic field alignment of R1 relative to R2 was favorable for reconnection between the external loops of each region. The reconnecting loops contain already enriched plasma but it is also possible that the Alfvén waves generated by reconnection may have stimulated the enrichment (e.g., Laming 2004, 2015).

Finally, the plasma composition within the two largest EFRs had non-Gaussian distributions ranging from photospheric to coronal FIP bias (Figure 9). The distributions were mildly skewed toward the higher end of the distributions, with 32%–36% of the pixels within the masked regions exceeding

FIP bias = 2. The lower end of the range of FIP bias values was consistent with previous observations of FIP bias in newly emerged loops (Sheeley 1995, 1996; Widing & Feldman 2001; Laming 2015) and with studies of plasma composition in CHs (Feldman et al. 1998; Brooks & Warren 2011; Laming 2015), whereas the upper end of the range, $\sim$3, was lower than the levels typically found in quiescent AR cores, $\sim$3–4 (e.g., Baker et al. 2015; Del Zanna et al. 2015). The fraction of pixels containing FIP bias $>$3 was small in these regions: $\sim$4% for R1 and $\sim$1% for R2. The extent to which plasma is enriched is likely to be affected by the CH environment. EFRs are partially or fully surrounded by CH field containing a large reservoir of unmodified photospheric-composition plasma. Interchange reconnection between the closed loops of the EFRs and the open field of the CHs creates pathways for mixing of coronal and photospheric plasmas, and as a consequence, the enhancement of FIP bias may be modulated (Baker et al. 2013, 2015).

6. Conclusions

We analyzed the temporal evolution and spatial distribution of coronal plasma composition within flux regions of varying sizes located inside an equatorial coronal hole using observations from *Hinode*/EIS. We obtained FIP bias measurements in seven EFRs during different phases of their lifetimes. In general, plasma was enriched from a photospheric level to values greater than the quiet Sun in less than one day from the initial flux emergence. FIP bias remained steady for 1–2 days before declining during the decay phase to the photospheric composition of the surrounding coronal hole.

The spatially resolved composition map revealed how FIP bias was distributed in and around the small flux regions located in the CH. Plasma containing FIP bias in the range 2–3$^+$ was concentrated in core loops and in the area where interconnecting loops were formed by reconnection between loops of neighboring EFRs. At the interface between open and closed field, plasma mixing appeared to occur where reconnection took place between EFR closed loops containing enriched material and the surrounding coronal hole filled with photospheric plasma. We conclude that the variation in plasma composition, observed in all sizes of flux regions, from ephemeral regions to ARs, is affected by the magnetic topology of each region in its surrounding environment.

The spatial distribution of FIP bias in the composition map of ephemeral-like EFRs is similar to that of the anemone AR in Baker et al. (2015), which is up to an order of magnitude larger in magnetic flux content. Conversely, the rate of composition change from coronal to photospheric observed during the magnetic decay phase of the EFRs is significantly faster compared to that of larger ARs (Baker et al. 2015; Ko et al. 2016). Not only is the magnetic flux decay rate faster for the EFRs, but the so-called basal FIP bias level is photospheric in the coronal hole ($\sim$1), rather than $\sim$1.5 in the quiet Sun. Furthermore, EFRs are readily reconnected with the surrounding field, as their weak magnetic fields are more affected by the convection, which disperses the magnetic field more efficiently than in ARs.

In general, our results indicate that mean FIP bias increases during the magnetic emergence and early-decay phases, while it decreases during the magnetic late-decay phase. The rate of increase during the emergence phase is likely to be linked to the fractionation mechanism and transport of fractionated plasma that lead to the observed coronal FIP bias, holding true

for three orders of magnitude in magnetic flux from ephemeral-like EFRs to large ARs. On the other hand, the rate of decrease in mean FIP bias during the decay phase depends on the rate of reconnection with the surrounding magnetic field and the composition of the surrounding corona.

ORCID iDs

Deborah Baker ⓘ https://orcid.org/0000-0002-0665-2355
David H. Brooks ⓘ https://orcid.org/0000-0002-2189-9313
Lidia van Driel-Gesztelyi ⓘ https://orcid.org/0000-0002-2943-5978
Alexander W. James ⓘ https://orcid.org/0000-0001-7927-9291
Pascal Démoulin ⓘ https://orcid.org/0000-0001-8215-6532
David M. Long ⓘ https://orcid.org/0000-0003-3137-0277
Harry P. Warren ⓘ https://orcid.org/0000-0001-6102-6851
David R. Williams ⓘ https://orcid.org/0000-0001-9922-8117

References

Baker, D., Brooks, D. H., Démoulin, P., et al. 2013, ApJ, 778, 69
Baker, D., Brooks, D. H., Démoulin, P., et al. 2015, ApJ, 802, 104
Brooks, D. H., Baker, D., van Driel-Gesztelyi, L., & Warren, H. P. 2017, NatCo, 8, 183
Brooks, D. H., Ugarte-Urra, I., & Warren, H. P. 2015, NatCo, 6, 5947
Brooks, D. H., & Warren, H. P. 2011, ApJL, 727, L13
Brooks, D. H., & Warren, H. P. 2012, ApJL, 760, L5
Brooks, D. H., Warren, H. P., Williams, D. R., & Watanabe, T. 2009, ApJ, 705, 1522
Cheung, M. C. M., & Isobe, H. 2014, LRSP, 11, 3
Culhane, J. L., Brooks, D. H., van Driel-Gesztelyi, L., et al. 2014, SoPh, 289, 3799
Culhane, J. L., Harra, L. K., James, A. M., et al. 2007, SoPh, 243, 19
Dahlburg, R. B., Laming, J. M., Taylor, B. D., & Obenschain, K. 2016, ApJ, 831, 160
Del Zanna, G. 2013, A&A, 558, A73
Del Zanna, G., Dere, K. P., Young, P. R., Landi, E., & Mason, H. E. 2015, A&A, 582, A56
Del Zanna, G., & Mason, H. E. 2014, A&A, 565, A14
Del Zanna, G., & Storey, P. J. 2012, A&A, 543, A144
Dere, K. P., Landi, E., Mason, H. E., Monsignori Fossi, B. C., & Young, P. R. 1997, A&AS, 125, 149
Doschek, G. A., & Warren, H. P. 2016, ApJ, 825, 36
Doschek, G. A., & Warren, H. P. 2017, ApJ, 844, 52
Doschek, G. A., Warren, H. P., & Feldman, U. 2015, ApJL, 808, L7
Fazakerley, A. N., Harra, L. K., & van Driel-Gesztelyi, L. 2016, ApJ, 823, 145
Feldman, U., & Laming, J. M. 2000, PhyS, 61, 222
Feldman, U., Schühle, U., Widing, K. G., & Laming, J. M. 1998, ApJ, 505, 999
Freeland, S. L., & Handy, B. N. 1998, SoPh, 182, 497
Fu, H., Madjarska, M. S., Xia, L., et al. 2017, ApJ, 836, 169
Gloeckler, G., & Geiss, J. 1989, in AIP Conf. Ser. 183, Cosmic Abundances of Matter, ed. C. J. Waddington (Melville, NY: AIP), 49
Grevesse, N., Asplund, M., & Sauval, A. J. 2007, SSRv, 130, 105
Harvey, K. L. 1993, PhD thesis, Univ. Utrecht
Harvey, K. L., Harvey, J. W., & Sheeley, N. R., Jr. 1982, SoPh, 79, 149
Hofmeister, S. J., Veronig, A., Reiss, M. A., et al. 2017, ApJ, 835, 268
James, A. W., Green, L. M., Palmerio, E., et al. 2017, SoPh, 292, 71
Kamio, S., Hara, H., Watanabe, T., Fredvik, T., & Hansteen, V. H. 2010, SoPh, 266, 209
Kashyap, V., & Drake, J. J. 2000, BASI, 28, 475
Ko, Y.-K., Young, P. R., Muglach, K., Warren, H. P., & Ugarte-Urra, I. 2016, ApJ, 826, 126
Kosugi, T., Matsuzaki, K., Sakao, T., et al. 2007, SoPh, 243, 3
Krista, L. D., & Gallagher, P. T. 2009, SoPh, 256, 87
Laming, J. M. 2004, ApJ, 614, 1063
Laming, J. M. 2009, ApJ, 695, 954
Laming, J. M. 2012, ApJ, 744, 115
Laming, J. M. 2015, LRSP, 12, 2
Laming, J. M., Drake, J. J., & Widing, K. G. 1995, ApJ, 443, 416
Lang, J., Kent, B. J., Paustian, W., et al. 2006, ApOpt, 45, 8689
Lanzafame, A. C., Brooks, D. H., Lang, J., et al. 2002, A&A, 384, 242
Lemen, J. R., Title, A. M., Akin, D. J., et al. 2012, SoPh, 275, 17
Longcope, D. W., & Fisher, G. H. 1996, ApJ, 458, 380
Mandrini, C. H., Nuevo, F. A., Vásquez, A. M., et al. 2014, SoPh, 289, 4151
Morgan, H., & Druckmüller, M. 2014, SoPh, 289, 2945
Pesnell, W. D., Thompson, B. J., & Chamberlin, P. C. 2012, SoPh, 275, 3
Raassen, A. J. J., Ness, J.-U., Mewe, R., et al. 2003, A&A, 400, 671
Scherrer, P. H., Schou, J., Bush, R. I., et al. 2012, SoPh, 275, 207
Schou, J., Scherrer, P. H., Bush, R. I., et al. 2012, SoPh, 275, 229
Sheeley, N. R., Jr. 1995, ApJ, 440, 884
Sheeley, N. R., Jr. 1996, ApJ, 469, 423
Telleschi, A., Güdel, M., Briggs, K., et al. 2005, ApJ, 622, 653
van Driel-Gesztelyi, L., Culhane, J. L., Baker, D., et al. 2012, SoPh, 281, 237
van Driel-Gesztelyi, L., & Green, L. M. 2015, LRSP, 12, 1
Warren, H. P. 1999, SoPh, 190, 363
Widing, K. G. 1997, ApJ, 480, 400
Widing, K. G., & Feldman, U. 2001, ApJ, 555, 426
Wood, B. E., & Linsky, J. L. 2010, ApJ, 717, 1279
Young, P. R., Del Zanna, G., Mason, H. E., et al. 2007, PASJ, 59, S857
Young, P. R., Watanabe, T., Hara, H., & Mariska, J. T. 2009, A&A, 495, 587